Response of near-inertial energy to a supercritical tropical cyclone and jet stream in the South China Sea: modeling study

Hiu Suet Kung, Jianping Gan*

Department of Ocean Science and Department of Mathematics, Hong Kong University of Science and Technology, Hong Kong

Corresponding author: magan@ust.hk

ABSTRACT

We used a well-validated three-dimensional ocean model to investigate the process of energetic response of near-inertial oscillations (NIOs) to a tropical cyclone (TC) and strong background jet stream in the South China Sea (SCS). We found that the NIO and near-inertial kinetic energy (KEni) varied distinctly during different stages of the TC forcing, and the horizontal and vertical transport of KEni was largely modulated by the velocity and vorticity of the jet stream. The KEni reached its peak value within ~one-half the inertial period after the initial TC forcing stage in the upper layer, decayed quickly by one-half in the next two days, and further decreased in a slower rate during the relaxation stage of the TC forcing. Analyses of the KEni balance indicate that the weakened KEni in the upper layer during the forcing stage was mainly attributed to the downward KEni transport due to pressure work through the vertical displacement of isopycnal surfaces, while upward KEni advection from depths also contributed to the weakening in the TC-induced upwelling region. In contrast, during the relaxation stage as TC moved away, the effect of vertical advection on KEni reduction was negligible and the KEni was chiefly removed by the outward propagation of inertial-gravity waves, horizontal advection and viscous dissipation. Both the outward wave propagation and horizontal advection by the jet stream provided the KEni source in the far-field. During both stages, the negative geostrophic vorticity south of the jet stream facilitated the vertical propagation of inertial-gravity waves.

1 Introduction

Near-inertial oscillations (NIOs), whose frequencies are close to the local inertial frequency contain around half of the observed internal wave kinetic energy in the ocean (Simmons and Alford, 2012). NIOs also greatly affect the kinetic energy budget in the deeper ocean as they propagate downward from the surface and enhance the mixing by increasing vertical shear (Gill, 1984; Gregg et al., 1986; Ferrari and Wunsch, 2009; Alford et al., 2016).

Tropical cyclones (TCs), with the rapid change of wind stress, provide an important generation mechanism for the NIOs. Observational studies related to a single storm or tropical cyclone (Price, 1981; Shay and Elsberry, 1987; D'Asaro et al., 1995) showed that the NIOs related to TCs can be a factor 2-3 larger than the background NIOs and last for more than 5 inertial periods (IPs). Using a hurricane-ocean coupled model, Liu et al. (2008) estimated that the energy input of tropical cyclones into the near-inertial currents was about 0.03 TW, about 10% of the total wind-induced near-inertial energy (Watanabe and Hibiya, 2002; Alford, 2003). The input of wind energy to the near-inertial band is also controlled by the translation speed of the TC (U_h) (Geisler, 1970; Price, 1981). In fact, the NIOs are largely variable during the forcing and relaxation stage of the TC forcing related to the intensity and translation speed of the TC. The variation is determined not only by the different magnitude of input of wind energy, but also by the different dynamic conditions that regulate the near-inertial kinetic energy (KEni) transport during these stages. The variable response of NIOs during different stage of TC forcing is critical for understanding the process and physics of NIOs.

Once generated, the characteristics of NIOs, in terms of the decay time scale, propagation direction, and propagation speed are influenced by various mechanisms. In linear wave theory, the β-effect leads to an equatorward propagation of the NIOs and reduces its decay time scale because

of the vertical propagation into deeper ocean (Gill, 1984; D'Asaro, 1989; Garrett, 2001). Background flow fields also impose large influence on the evolution of NIOs. The influence of background vorticity on NIOs has been observed by Weller (1982) and Kunze and Sanford (1984), and analytical proofs by Kunze (1985), Young and Ben Jelloul (1997), and Danioux et al. (2015). Numerical study using a primitive equation model with a turbulent mesoscale eddy field and uniform wind forcing gave a similar conclusion (Danioux et al., 2008). Non-linear interactions also provide a mechanism for increasing the vertical wave number, thus for larger vertical shear and the dissipation and reducing the decay time scale (Davies and Xing, 2002; Zedler, 2009). In addition to modifying the characteristics of the inertial-gravity waves, nonlinear advection related to the front can transport NIOs away from the storm track and to higher latitudes (Zhai et al., 2004). Recent observations and numerical studies in Gulf Stream, Kuroshio, and Japan Sea revealed the role of vertical circulation on the generation and radiation of near inertial energy (Whitt and Thomas, 2013; Nagai et al., 2015; Rocha et al., 2018; Thomas, 2019).

The South China Sea (SCS) is a region with frequent tropical cyclone occurrence, ~10.3 each year (Wang et al., 2007). Observations (Sun et al., 2011a, b; Xu et al., 2013) and numerical studies (Chu et al., 2000) indicated that these TC events are sources for near-inertial energy bursts. Additionally, the SCS circulation contains abundant energetic flow (e.g. Qu, 2000; Gan et al., 2006; Gan et al., 2016a) and mesoscale features, such as a strong coastal jet off the Vietnamese coast (e.g. Gan and Qu, 2008) and eddies (e.g. Chen et al., 2012). The distribution and evolution of the TC-induced NIOs are susceptible to the influence of these background currents. (Sun et al., 2011a; Sun et al., 2011b). However, the estimate of the total contribution of a TC to the KEni in the SCS is difficult to obtain from observations or linear wave theory due to sparse spatial observations and the non-homogenous nature of SCS circulation.

In this study, we apply a well-validated numerical model with specific China Sea configurations to examine the response of KEni to a large TC and background stream jet over the sloping topography in the SCS. A description of Typhoon Neoguri and the details of the numerical model implementation are given in Section 2. In Section 3, the general characteristic response of the near-inertial current and the energy fluxes during the TC forced stage and their later relaxation stage as TC moved away from the concerned region are presented. Following Section 3, the KEni equation is used to identify the dynamic processes of the vertical viscous dissipation, pressure work, and nonlinearity during different phases of the NIOs.

2 Typhoon Neoguri (2008) and the Ocean Model

2.1 Typhoon Neoguri (2008)

Typhoon Neoguri formed east of the Philippines and entered the SCS on April 15. It first moved west-northwest with an average translation speed of 5.8 m s^{-1} before it slowed down to 1.6 m s^{-1} on April 16, based on the Joint Typhoon Warning Center (JTWC) best track data, (Fig. 1). On April 17, Neoguri sped up to 3.8 m s^{-1}, turned more northward, and developed into a typhoon with a maximum wind speed 51 m s^{-1} and a MSLP (minimum sea level pressure) at 948 hPa, at 1800 UTC on April 17 near the Xisha Islands. The Neoguri was a supercritical typhoon travelling with a translation speed greater than the first baroclinic wave speed. After skirting Hainan Island on April 18, Neoguri moved northward, weakened to a tropical storm, and further dissipated as it moved farther inland. The NIO burst induced by Neoguri was shown by the clockwise (A_{cw}) and counter-clockwise (A_{ccw}) rotary current amplitudes (m s^{-1}), from a current meter mooring at Wenchang station, to the east off Hainan Island (Fig. 1c).

2.2 Ocean Model

We use the China Sea Multi-scale Ocean Modeling System (CMOMS) (Gan et al., 2016a; Gan et al., 2016b) in this study. CMOMS is based on the Regional Ocean Modeling System (ROMS) (Shchepetkin and McWilliams,2005), and the model domain covers the northwest Pacific Ocean (NPO) and the entire China Seas (Bohai, Yellow Sea, East China Sea, and SCS) from approximately 0.95ºN, 99ºE in the southwest corner to the northeast corner of the Sea of Japan. The horizontal size of this grid array decreased gradually from ~10 km in the southern part to~7 km in the northern part of the domain. Vertically, we adopted a 30-level stretched generalized terrain-following coordinate (s).

The model was forced with 6-hourly actual wind speeds of typhoon Neoguri obtained from the Cross-Calibrated Multi-Platform (CCMP) dataset, with a horizontal resolution of 0.25° (Atlas et al. (2011), ftp://podaac-ftp.jpl.nasa.gov/allData/ccmp/L3.0/flk). Wind stress is calculated based on the bulk formulation by Fairall et al. (2003). The daily mean air temperature, atmospheric pressure, rainfall/evaporation, radiation, and other meteorological variables from April 15 to April 18, 2008 from the NCEP/NCAR Reanalysis 1 were used to derive the atmospheric heat and fresh fluxes. External forcing of depth-integrated velocities (*U, V*), depth-dependent velocities (*u, v*), temperature, *T*, and salinity, *S*, at the lateral boundaries were obtained from the Ocean General Circulation Model for the Earth Simulator (OFES) (Sasaki et al., 2008). Open boundary conditions from Gan and Allen (2005) were applied at the open boundaries.

The model was spun up from January 1, 2005 with winter initial fields (temperature and salinity) obtained from the last three-year mean fields of a 25-year run that is initialized with the World Ocean Atlas 2005 (WOA05, Locarnini et al., 2006, Antonov et al., 2006) data, and forced by wind stress derived from climatological (averaged from 1988 to 2013) monthly Reanalysis of

10 m Blended Sea Winds released by the National Oceanic and Atmospheric Administration (https://www.ncdc.noaa.gov/oa/rsad/air-sea/seawinds.htm). The dynamic configuration and numerical implementation of the CMOMS system are described in detail in Gan et al. (2016a, 2016b).

We have thoroughly validated the CMOMS by comparing simulated results with those obtained from various measurements and findings in previous studies. In particular, we have validated the extrinsic forcing of time-dependent, three-dimensional current system in the tropical NPO, transports through the straits around the periphery of the SCS, and corresponding intrinsic responses of circulation, hydrography and water masses in the SCS (Gan et al., 2016a). We have also validated the circulation of CMOMS by providing a consistent physics between the intrinsic responses of the circulation and extrinsic forcing of flow exchange with adjacent oceans (Gan et al., 2016b). The model is also validated with available ARGO temperature profiles (not shown), observed sea surface temperature (SST) and currents from a time-series current meter mooring during Neoguri, as described below.

Three-dimensional, hourly-mean dynamic, and thermodynamic variables from April 10 to May 10, 2008 were used to examine the near-inertial oscillations in this study. Because the inertial period (IP) in the SCS is larger than 32 hours (near 22°N), the error induced by the hourly model output is <3%.

3 Model result

3.1 Characteristic response to the TC

The evolution of the response to the TC in the ocean with existence of a coastal jet in the SCS is presented according to different stages of the TC forcing. During the pre-storm stage (PS), before Neoguri entered the SCS on April 14, the wind stress was relatively weak (<0.1 Pa). A

prominent jet current separated from the Vietnamese coast flowing northeastward near 16°N (Fig. 2a), and characterized the circulation in the western part of the SCS. The jet stream was resulting from the (summer) monsoon-driven strong coastal current over narrow shelf topography off Vietnam and it persisted as a distinct circulation feature in the SCS during summer. The northward flowing coastal current separated from the coast and overshoots northeastward into the SCS basin as it encountered the coastal promontory in the central Vietnam (Gan and Qu, 2008).

The jet formed negative (positive) geostrophic vorticity (ζ_g) to the south (north), with the minimum (maximum) Rossby number (ζ_g/f) <-0.2 (>0.2) near 15.8°N (16.8°N). During the forced stage (FS, Fig. 2b) between April 15 and April 19, the SCS was under the direct influence of Neoguri, the wind forcing became significantly stronger (>0.1 Pa), the KE near the surface (10 m) intensified significantly (>500 J m^{-3}) to the east of the TC, and the coastal jet was suppressed by southward flow. Meanwhile, a strong local divergence and upwelling formed in the surface and generated a strong cooling (~1.5°C) belt along the TC path that lasted for more than a week. The cooling zone radiated hundreds of kilometer away from the core of the TC. These features were well captured by the TC-induced temperature difference between April 19 and 14 from both simulated (Fig. 3a) and observed SST (Fig. 3b) (http://podaac.jpl.nasa.gov/dataset/JPL-L4UHfnd-GLOB-MUR). After the end of the FS on April 20 (Fig. 2c), the jet returned to its pre-storm intensity and shifted slightly northward (Fig. 2c) when the TC center approached the coast (Fig. 1a). Afterwards, during the relaxation stage (RS) after April 20 (Fig. 2d), the wind forcing from the TC decreased to <0.05 Pa.

Rotary spectra shows that the near-inertial response of surface currents to the TC occurred near the local inertial frequency (f = 0.028 cph) at station Wenchang (112°E, 19.6°N) during the

model simulation period (April 10 – May 5) (Fig. 4). The clockwise rotary spectra is calculated by:

$$S_{cw} = 1/8(P_{uu} + P_{vv} - 2Q_{uv}), \quad (1)$$

where P_{uu}, P_{vv} and Q_{uv} are auto- and quadrature-spectra, respectively (Gonella, 1972). This simulated result is highly consistent with the observations in the lower frequency band. We found that the correlation coefficients of near-inertial band-passed velocity between ADCP and model simulation at Wenchang station were 0.62 and 0.57 for east-west (u) and north-south (v) component, respectively, which indicated that the model captured reasonably well the NIOs under the influence of the background circulation of the SCS. There existed inevitably the model-observation discrepancies, such as differences of velocity magnitude (~0.06 m s^{-1}) at near-inertial band and rotary spectra at the higher frequency (Fig. 4). The discrepancies could have been caused by many reasons, such as the lack of mesoscale and sub-mesoscale processes in the atmospheric forcing field, the linear interpolation process of the atmospheric forcing (Jing et al., 2015), and not resolving the oceanic subscale processes by the current model resolution. However, these discrepancies will not undermine the discussion about the process and mechanism of near-inertial energy response to the TC and jet stream in this study.

3.2. Near-inertial response in the upper ocean

We adopted the complex demodulation method successfully used in previous NIO studies (Gonella, 1972; Brink, 1989; Qi et al., 1995) to extract the inertial current signal. The simulated horizontal currents ($\vec{u}_h$) were analyzed for inertial currents ($\vec{u}_i$). The inertial currents contain clockwise (cw) and counter-clockwise (ccw) rotating components:

$$u_i + iv_i = A_{cw}e^{-i(\phi_{cw}+ft)} + A_{ccw}e^{i(\phi_{ccw}+ft)}, \quad (2)$$

where u_i and v_i are the eastward and northward inertial currents at 10 m in the mixed layer, A and ϕ are the amplitude and phase of the rotary currents, respectively. Subscripts represent the clockwise (*cw*) and counter-clockwise (*ccw*) rotating direction, and f is the local Coriolis coefficient. To obtain the amplitude and phase, we performed harmonic analysis daily with each segment over one inertial period (IP). Then the rotary amplitude and phase were calculated following previous studies (Mooers, 1973, Qi et al., 1995, Jordi and Wang, 2008).

The time evolution of the daily rotary currents during the FS and RS in the surface layer varied spatially and was related to the intensity and translation speed of the TC. On April 15 during PS, Neoguri affected mainly the region south of 13°N, with a relatively fast translation speed ($U_h > 3C_1$, Fig. 1b) and weaker intensity (V_{max}~35 m s^{-1}). In most areas, *cw* rotary currents were strong (A_{cw} >0.1 m s^{-1}) yet decayed quickly after 3 days (<2 IP) (Fig. 5a), while the magnitudes of *ccw* currents were very small (Fig. 5b). After April 18, Neoguri moved into the region between 14°N and 18°N, where it intensified more than 40% but moved slower with U_h~2C_1. Both the *cw* and *ccw* currents possessed larger intensities than in the southern region. The induced *cw* currents displayed an obvious rightward bias, where the enhanced inertial currents extended to ~350 km to the right of the track and to ~<150 km to the left of the track. This extension of horizontal scale was related to the region with wind stress $|\boldsymbol{\tau}|$>0.25 Pa in Neoguri.

The maxima of the *ccw* component were located to the left of the TC's path where the wind vector (Fig. 6) rotated in the same direction as the ocean currents presented in Fig. 5. The connection between the right (left) bias of the *cw* (*ccw*) currents with the rotation direction of the wind vector is in agreement with the explanation of Price (1981). 2-3 IPs (>6 days) after the direct forcing, the *cw* currents remained significant (>0.2 m s^{-1}) in an area extending from 110°E to 116°E. In contrast, the *ccw* components, which rotated in the direction of the Earth's rotation,

dissipated quickly after the wind forcing stopped within ~1 day. This short duration of the forced inertial motion is in agreement with previous studies (Jordi and Wang, 2008).

Besides the intensity and duration, we also looked at the frequency shift ($\delta\omega=\omega-f$) and the horizontal scale of the NIOs. The frequency shift from the local inertial frequency was estimated from the temporal evolution of the phase of the back rotary current: $\delta\omega=-\partial\phi/\partial t$. In the FS, the maximum frequency shift occurred near the jet (112°E to 115°E, 15°N to 16°N), where $\delta\omega\approx0.08f$ ($\Delta\phi\approx\pi/4$,Δt=3 days, f=4×10^{-5} s^{-1} at 16°N). The horizontal scale was estimated from the spatial variation of the rotary current by calculating the horizontal wave number in the meridional direction as $k_y=\partial\phi/\partial y$. The largest wave number $k_y \approx 3.1\times10^{-5}$ rad m^{-1} was also found near the jet.

3.3 Characteristic near-inertial energy

Response in the upper layer

We focused on the area between 110-115°E and 13-19°N (box in Fig. 5a), defined as the forced region, where the strongest NIO was produced during FS of Neoguri. We calculated the wind-induced near-inertial energy flux (or the wind work) using $\vec{\tau}_i \cdot \vec{u}_i$, where $\vec{\tau}_i$ is the band-passed near-inertial wind stress and $\vec{u}_i$ is the near-inertial current at the surface (Silverthorne and Toole, 2009). A 4th order elliptic band-pass filter (Morozov and Velarde, 2008) was applied to obtain near-inertial motion with a band ranging from 0.8f to 1.2f, where f is the local Coriolis coefficient. The time series of domain-averaged $\vec{\tau}_i \cdot \vec{u}_i$ over the forced region reveals that significant energy input took place during the FS, with the peak value about 68×10^{-3} W m^{-2} on April 17 (Fig. 7). Under this large wind energy input, the area-averaged depth-integrated KEni (or *AKEni* hereafter) in the upper layer (0-30 m) increased significantly from its pre-storm value to a maximum ~1500 J m^{-2} during the FS, with an increase rate of about 16×10^{-3} W m^{-2} (Fig. 7a). Despite the continuous

223 positive wind energy flux, the *AKEni* in the upper layer plateaued, indicating that a large amount
224 of the wind energy was either propagating out the forced region or was lost to the lower layers due
225 to entrainment. The detailed mechanisms are discussed in the following sections. After the peak
226 of FS, the wind work decreased significantly with small negative value around the end of the FS.
227 The *AKEni* decreased to one half of its peak value within 2 days (decrease rate was about 7×10^{-3}
228 W m^{-2}). After that, the wind work was almost negligible, and the decrease rate of *AKEni* became
229 smaller (~0.8×10^{-3} W m^{-2}).

230 ***Response at depths***

231 During the FS, the *AKEni* in the upper 200 m constituted ~90% of the total *AKEni* in the
232 whole water column, while the *AKEni* between 30-200 m alone accounted for ~30-50% (Fig. 7b).
233 The KENI in this mid-layer had a temporal evolution different from that in the near surface layer.
234 It reached its maximum on April 20, around one and a half days later, and was more than 80% of
235 the peak value of the *AKEni* in the upper layer (~1000 J m^{-2}). Compared to the upper layer *AKEni*,
236 the the mid-layer *AKEni* during FS increased slightly more slowly (~ 4×10^{-3} W m^{-2}) while from
237 April 20 to May 5 during RS it decreased much more slowly (~0.61×10^{-3} W m^{-2}), and the *AKEni*
238 became greater than that in the upper layer at the end of FS. The *AKEni* below 200 m was much
239 smaller, but increased continuously from April 17 to 29, with a rate of about 0.62×10^{-3} W m^{-2},
240 which was comparable to the *AKEni* rate of decrease in the 30-200 m layer. The *AKEni* in this
241 deep layer became greater than that in the upper layer after April 25 and that in the layer 30-200
242 m after April 29; the deep layer reached its maximum value >10 days later.

243 Spatially, two relatively large KEni patches below upper layer were located to north and
244 south of ~16°N (Fig. 8a). Their horizontal scales, influenced by near-inertial waves, were much
245 smaller compared with those in the upper layer. The region with relatively large KEni in the layer

between 30-200 m located near the jet currents, with stronger value during FS than during RS (Fig. 8 a,b). These results suggest that the KEni in this layer might have been determined by both vertical propagation of the near-inertial gravity wave and horizontal advection of KEni of the background current. Similar horizontal distribution also occurred below 200 m (Fig. 8 c,d). In contrast to the layer above, the relatively large value during RS on April 30 indicated a downward propagation of KEni into the deeper layer. Around the saddle zone west of the Xisha Islands, a relatively large KEni below 200 m aligned with the 1000 m isobath, and might reflect a topographic effect on the near-inertial wave.

3.4 Vertical propagation of near-inertial energy

It is clear that the distribution of the KEni was mainly controlled by the propagation of near-inertial wave energy both horizontally and vertically as well as by the background jet stream. In order to understand the KEni distribution in the deeper water inside the forced region and in the far field, we selected four different locations, marked as A1, A2, C1, and C2 in Fig. 8 (a-d), for the analysis of the KEni evolution during the FS and RS. Among them, A1 (113°E, 15.7°N) and A2 (112.5°E, 16.9°N) are on the right side of the TC track, inside the forced region, and situated about 200 km apart from each other at the northern (A2) and southern (A1) sides of the jet, respectively. C1 (114.9°E, 16.9°N) and C2 (114.9°E, 18°N) are the corresponding stations in the far field where relatively strong KEni intensification occurred.

Forced region (stations A1 and A2)

South of the jet stream at station A1

The time series of the band-passed inertial velocity u_i as a function of depth shows that there was an upward phase propagation, in which u_i, in the layers below 100 m was leading the upper 50 m (Fig. 9a). Accompanying this phase propagation was a downward propagation of surface KEni,

which was represented by the lowering of the u_i maxima as a typical Poincaré wave (Kundu and Cohen, 2008). There were two phases of vertical energy propagation: 1) during FS, there was a rapid extension of the large u_i maxima to below 100 m from April 17 to 20, and 2) during RS, the center of the large u_i value descended from ~100 m to 280 m from April 25 to May 5. The vertical propagation velocity, C_{gz}, estimated from this downward transport, was ~17 m day^{-1}.

During the first phase, the KEni in the top 30 m and in the 30-200 m layer shared a similar rate of increase on April 17, indicating that the enhancement of KEni at 30-200 m was related to the entrainment between the upper and deep layer (Fig. 9c). While the KEni in the upper 30 m decreased quickly from April 18, it kept increasing at depths from 30-200 m, suggesting that other contributing mechanisms existed besides the entrainment. The KEni below 200 m also experienced notable intensification, with a smaller increasing rate than that found in the 30-200 m layer (Fig. 9c). Because the viscous effect is small in the deeper water, this enhancement of the KEni was most likely associated with the propagation of an inertial-gravity wave.

During the second phase, the KEni in the 30-200 m layer decreased significantly at station A1, indicating the existence of either downward or horizontal energy transport. From the linearized inertial-gravity wave equation under the influence of background vorticity, C_{gz} can be obtained by (Morozov and Velarde, 2008),

$$C_{gz} = \frac{\omega^2 - f_{eff}^2}{\omega m}, \quad (3)$$

where $\omega \approx 1.08f$ is the frequency with maximum S_{cw} at 200 m (Fig. 9e); $f_{eff}=f+\zeta_g/2$ is the effective Coriolis coefficient; and ζ_g/f=-0.1 at A1. m is the vertical wave number that we chose to be the first baroclinic mode under a two-layer approximation based on the stratification (blue line in Fig. 10a). From Eq. (3), C_{gz} was about 19.1 m day^{-1}, which was in the same range as the modeled C_{gz}. Consistent with the case of $(\omega_0-f_{eff})/f_{eff}$<0.1 in Kunze (1985), the background vorticity in our case

accounted for more than 90% of the modification of the magnitude of the wave dispersion property. Meanwhile, the KEni in the layer below 200 m did not increase notably, suggesting that other mechanisms besides vertical propagation of the near-inertial gravity wave might have been important in the evolution of KEni in water deeper than 200 m.

North of the jet stream at station A2

At location A2, strong u_i was mainly trapped in the water above 100 m, and below 100 m u_i <10 cm s^{-1}. It returned to its pre-storm magnitude after 5 IPs (Fig. 9b). This constrain of vertical propagation is likely associated with the vertical scale of the strong positive background vorticity (Fig. 10b). The KEni was generally smaller than that at A1, and relatively large energy was found only in the ML (Fig. 9d). C_{gz} at A2, estimated from Eq. (3), was 2.1 m day^{-1} (f_{eff}=1.08f, ω≈1.1f, f=4.2×$10^{-5}$$s^{-1}$, and m=2π/30 m), which was about one tenth of that at A1. This is consistent with the lack of a distinct pattern of vertical propagation of NIOs at this station, as shown in the band-passed u_i (Fig. 9b), and the presence (absence) of a near-inertial peak of S_{cw} at 10 m (200 m) (Fig. 9f).

Far field region (stations C1 and C2)

C1 and C2 are located ~400 km to the right of the forced region. During the FS, u_i (Fig. 11a,b) and KEni (Fig. 11c,d) in the upper layer were smaller than those at those stations in the forced region due to the weaker TC influence. Only a small downward propagation was discerned during the FS (Fig. 11a,b). However, notable intensification of the KEni occurred in the layers below the upper layer after April 23. At C1, the S_{cw} at 10 m had a small red shift, while the S_{cw} at 200 and 500 m displayed blue shifts with peaks near 1.07f (Fig. 11e). The difference between S_{cw} in the upper layer and in the layers below implies another source of KEni other than local inertial-gravity wave vertical propagation.

At C2, downward energy propagation appeared after April 23, reaching 100 m from the surface within 7 days, giving C_{gz} =14.3 m day^{-1} (Fig. 11b). Unlike C1, the intensification was mainly in the 30-200 m layer. The S_{cw} at both 10 m and 200 m had a broad energy band near the local f (Fig. 12f). Because ζ_g/f = -0.11 and f_{eff} = 1.06f, C_{gz} estimated from Eq. (3) had an upward propagation (C_{gz} =-5.4 m day^{-1}), which cannot explain the downward propagation here. The linearized wave theory, with the consideration of Doppler drift due to background currents, does not seem to be valid in this location. We will discuss this issue in the next section.

4 KEni Budget

We utilized the KEni equation to provide a further analysis of the source of KEni in the water column. Because the horizontal component of near-inertial kinetic energy is significantly larger than the vertical component (Hebert and Moum, 1994), we used the horizontal component to represent the KEni. The KEni budget can be obtained from the horizontal momentum equation. Following Silverthorne and Toole (2009), the energy equation becomes:

$$\underbrace{\frac{\partial KENI}{\partial t}}_{RATE} = \underbrace{-\vec{u}_i \cdot \langle \nabla_h p \rangle}_{PRES} \underbrace{-\rho_0 \vec{u}_i \cdot \langle \vec{u}_h \cdot \nabla_h \vec{u}_h \rangle}_{NLh} \underbrace{-\rho_0 \vec{u}_i \cdot \left\langle w \frac{\partial \vec{u}_h}{\partial z} \right\rangle}_{NLv} \underbrace{-\rho_0 \vec{u}_i \cdot \left\langle \frac{\partial}{\partial z}\left(\upsilon \frac{\partial \vec{u}_h}{\partial z} \right) \right\rangle}_{VVISC} \quad (4)$$

where *AKEni* is the area-averaged depth-integrated near-inertial energy; $\vec{u}_i$ and $\vec{u}_h$ are the near inertial velocity vector and horizontal velocity, respectively; p is pressure; ρ_0 is the reference density; ∇_h is the horizontal gradient operator; w is the vertical velocity; υ is the viscosity coefficient; and the angle bracket represents band-passed filtering on the near-inertial band. The *PRES* term on the right side of equation represents the pressure work on the *AKEni*, which is associated with the inertial-gravity wave propagation. NL_h and NL_v represent the horizontal and vertical divergence of energy flux that include the effects of 1) the advection of *AKEni* due to background currents and 2) the straining of the wave field due to the background shear currents.

Zhai et al. (2004) found that the geostrophic advection of *AKEni* contributed most of the NL_h and was the main mechanism for transporting the NIOs in the absence of baroclinic dispersion of inertial-gravity waves. It was also found to be more important than the dispersive processes along the Gulf Stream or shelf-break jet. *VVISC* is the vertical viscous effect. As before, we integrate the KEni vertically in three layers: the upper layer (0-30 m), the subsurface layer (30-200 m), and the deep layer (>200 m). In the following sections, the *AKEni* budget is considered in entire forced region (Fig. 5) as well as at the specific stations along the jet stream.

4.1. Mean balance

Figure 12 shows the time series of the *AKEni* budget over the entire forced region defined in Fig. 5. The time-averaged horizontal distributions of each term are presented in Fig. 13. During the FS, the increase of *AKEni* in the upper layer was mainly attributed to the wind energy input because the *VVISC* term was one order larger than the other terms, with a maximum of 30×10^{-3} W m^{-2} on April 17 (Fig. 12a). The time-integrated *VVISC* during the FS was 2.15×10^{3} J m^{-2} (Table 1). Stronger *VVISC* in the upper 30 m occurred in the region between 14°N and18°N (Fig. 13a) along the TC track with a rightward bias, similar to the distribution of current intensity (Fig. 5c). Like the wind work during the FS (Fig. 7a), *VVISC* became negative after April 19, indicating the *AKEni* removal by negative wind work. The influence of *VVISC* extended to the 30-200 m layer, and provided a positive energy flux (~1×10^{3} J m^{-2}) in this layer (Figs. 12b, 13b). The effect of *VVISC* in the deep layer was negligible (Fig. 12c).

Shortly (~1 day) after the large injection of KEni into the upper layer during the FS, the *PRES* became significant (Fig. 12a, Table 1) and its horizontal distribution resembled that of *VVISC* (Fig. 13a, d), suggesting that *PRES* radiated the KEni out of the forced region. It provided a negative KEni flux in the upper layer (-0.65×10^{3} J m^{-2}), which was largely compensated by the

360 positive flux in deeper layers (Table 1). This suggests that, during the FS, the main role of the
361 pressure work was to transport the KEni from the upper layer to the deep layers, and <15% of the
362 KEni was horizontally propagated outside the forced region.

363 During the RS, the *VVISC* was relatively small in the upper layer and it accounted for one
364 third of the *AKEni* removal in the layers below (Table 1). The *PRES* became a major sink for
365 *AKEni* in the ML (-0.85×10^3 J m^{-2}) and subsurface layer (-0.16×10^3 J m^{-2}), but was the major
366 source in the water below 200 m. The *AKEni* loss due to the horizontal wave propagation outside
367 the forced region was ~-0.42×10^3 J m^{-2}, accounting for about 40% of the total loss in the whole
368 water column.

369 Nonlinear advection terms had an important influence in the top 200 m but made little
370 contribution to the *AKEni* budget in the water below 200 m (Fig. 12, Table 1). The horizontal
371 effects of NL_h and NL_v in these layers were mainly limited to a smaller region, as compared to the
372 *VVISC* and the *PRES;* and their relatively large values occurred near the slope and the jet (Figs.
373 13).

374 In the upper layer, NL_h advected the KEni from the source region; NL_h had positive and
375 negative values on the eastern and western sides of the TC track, respectively (Fig. 13g). Similar
376 features, but with much weaker amplitude, were found in the layers below (Fig. 13h,i). During the
377 FS, in the 30-200 m layer, the domain-averaged NL_h was positive (0.21×10^3 J m^{-2}), indicating a
378 possible extraction of the KEni from background flows. NL_v was a strong energy sink in the upper
379 200 m (~0.64×10^3 J m^{-2}). The TC wind field generated a strong surface horizontal divergence and
380 upwelling around 16-17°N (Fig. 4b). As a result, the smaller KEni in the lower layer was advected
381 to the surface east of the Xiasha Islands. This lower KEni generated a negative gradient with
382 ambient water and resulted in the strong eastwards transport of KEni in the eastward jet current.

As a result, a positive NL_h center located around the area with the strongest negative NL_v, and a negative NL_h center lay to the west of the positive maximum of NL_h. During the RS, NL_h became negative for all layers and provided ~1/3 of the total KEni loss in the water column (-0.35×10^3 J m^{-2}), while NL_v over the whole water column was significantly reduced.

4.2 Role of the jet stream

We further show the distinct *AKEni* balance in the southern and northern sides of the jet stream. During the FS, *VVISC* at A1 on the southern side of the jet stream was the dominant *AKEni* source in both the upper layer and the 30-200 m layer (Fig. 14a,b), consistent with the large vertical scale on the southern side of the jet due to local negative vorticity. The enhancement of near-inertial currents in the upper layer and the concurrent current divergence resulted in the vertical oscillation of isopycnals (pressure) below the upper layer at this station. During this pumping process, the *AKEni* in the upper layer was partly transported downward by the *PRES* and partly by the NL_v. During the RS, the *PRES* became the main factor in the *AKEni* budget. It changed from source to sink in the 30-200 m layer, because of less downward KEni flux from the upper layer. In the deeper layer, the negative *PRES* indicated that there was a near-inertial wave propagating away from this location. The positive *AKEni* flux provided by NL_h weakened the effect of the negative *PRES*.

During the FS at A2 on the northern side of the jet stream, *VVISC* in the upper layer (Fig. 14d) had slightly larger magnitude than that at A1. However, it greatly decreased to 3×10^{-3} W m^{-2} below the ML (Fig. 14e), which suggested that the smaller vertical scale on the northern side of the jet limited the deep penetration of the wind energy in this location. Compared to A1, the NL_v was much stronger in the upper layer, and about one half of the lost energy was compensated for by the NL_h. The *PRES* was negligible compared to that at A1 (Fig. 14d-f). During the RS, the *PRES* in the ML became a notable sink after April 21 and was accompanied by a positive NL_h (Fig. 14d).

406 This suggests that the strong jet increased the *AKEni* through either advection or wave propagation
407 due to *PRES* as a result of jet-NIO interaction at this station. In the deeper layer, the *PRES* provided
408 a positive *AKEni* flux. From the spectral analysis, the wave at 500 m had a large blue shift of
409 >0.15*f* (Fig. 9f) that cannot be explained by the background vorticity alone. The wave likely
410 originated from the northern latitude.

411 In the far field at stations C1 and C2, where there was no direct wind forcing from the TC,
412 surface forcing (*VVISC*) was relatively small during the FS (Fig. 14g,j). Therefore, horizontal
413 transport of energy is needed to sustain the KEni intensification at these two locations (Fig. 11c,d).
414 At C1, which was on the southern side of the jet stream (Fig. 8) and had a negative background
415 vorticity, the *PRES* was the main source of *AKEni* in both subsurface and deep layers (Fig. 14h,i).
416 The existences of the blue shift near the local inertial frequency (Fig. 11e) and of the negative
417 background vorticity suggest the presence of a southward propagating near-inertial wave towards
418 C1 from northern region. Because C2 lies near the northeastward turning point of the jet (Fig. 8),
419 the nonlinear effect became significant in the 30-200 m layer where the jet was strongest (Fig.
420 14k). After the enhancement of *AKEni* in the subsurface layer, the *PRES* further transported the
421 KEni downwards and became the major source for the increase of *AKEni* in the deep layer after
422 April 27 (Fig. 14l). The northeast current advected the lower frequency NIO from the lower
423 latitude towards the higher latitude, C2, which explains the red shift of the NIO at this location
424 (Fig. 11f).

425 ## 5 Summary

426 TCs force the ocean to form NIOs. The response of NIOs is largely associated with the
427 different forcing stages of the TCs and background flow. Due to spatiotemporally limited
428 measurements, our understanding of the process and mechanism that govern the NIO response is

mainly based on theories that are constrained by idealized assumptions. In this study, we utilize a well-validated circulation model to investigate the characteristic response of KEni to a moderately strong TC (Neoguri) with observed strong KEni and to a unique background circulation.

The near-inertial currents in the upper layer strengthened significantly during the TC forced stage and displayed a clear rightward bias due to stronger wind forcing and the resonance between the wind and the near-inertial currents. The distribution of near-inertial currents and the associated rotary spectra showed that the propagation patterns of NIOs varied greatly from location to location and were closely linked to the influences of the background jet.

We calculated the KEni balance to diagnose spatiotemporally varying responses and processes of the near-inertial signals in terms of different forcing stages of the TC. Results show that during the forcing period, the vertical viscous term, which represents the wind work and entrainment at the base of the upper layer, was the KEni source in the upper layer. Around 0.5 IP after the maximum TC forcing, the pressure work became the main KEni sink in the upper layer, transporting KEni in the ML into the deeper layers through inertial pumping (upwelling). The upwelling, caused by the TC-enhanced divergence, also advected smaller KEni from deeper layers to weaken the KEni in the upper layer.

During the TC relaxation stage, the loss of KEni in the forced region of the whole water column were caused by the vertical viscous term, the pressure work, and horizontal advection effects (Table 1). However, these effects acted differently in different layers. The viscous effect mainly occurred inside the water column, but decreased to near zero in the upper layer after the direct impact of Neoguri. The pressure work mainly transported the KEni out of the forced region horizontally and out of the upper layer vertically. It was strongest on the southern side of the jet, where the negative background vorticity located. The horizontal nonlinear effect also contributed

greatly to the KEni balance near the jet region. It acted as a major sink of KEni by horizontally advecting the NIO away from the forced region. For locations away from forced region, both near-inertial wave propagation and horizontal advection contributed to the intensification of the KEni.

We examined the NIOs processes and underlying dynamics in response to different stage of the TC in the semi-enclosed SCS under influence of unique and strong basin-wide circulation. Unlike similar study in the SCS, this study enriches our understanding of the spatiotemporal variability of TC-induced NIOs and provides a useful physical guidance for future process-oriented field experiment in the SCS as well as in other subtropical marginal seas that are frequently affected by the TC.

Acknowledgments.

This research was funded by the General Research Fund of Hong Kong Research Grant Council (GRF16204915) and the Key Research Project of the National Science Foundation of China (41930539). The buoy data was provided by Qi He from CNOOC Energy Technology & Services Limited, China. We are also grateful for the support of The National Supercomputing Center of Tianjin and Guangzhou.

469 **References**
470
471 Alford, M. H., 2003: Improved global maps and 54-year history of wind-work on ocean inertial
472 motions. Geophys. Res. Lett., 30 (8), 1424, doi:10.1029/2002GL016614.
473 Alford, M. H., M. F. Cronin, and J. M. Klymak, 2012: Annual cycle and depth penetration of wind-
474 generated near-inertial internal waves at ocean station papa in the northeast pacific. J. Phys.
475 Oceanogr., 42, 889-908.
476 Alford, M.H., MacKinnon, J.A., Simmons, H.L. and Nash, J.D., 2016: Near-inertial internal
477 gravity waves in the ocean. Annu. Rev. Mar. Sci., 8(1), 95-123.
478 Antonov, J. I., R. A. Locarnini, T. P. Boyer, A. V. Mishonov, and H. E. Garcia, 2006. World Ocean
479 Atlas 2005, Volume 2: Salinity. S. Levitus, Ed. NOAA Atlas NESDIS 62, U.S. Government
480 Printing Office, Washington, D.C., 182 pp.
481 Atlas, R., R. N. Homan, J. Ardizzone, S. M. Leidner, J. C. Jusem, D. K. Smith, and D. Gombos,
482 2011: A cross-calibrated, multiplatform ocean surface wind velocity product for meteorological
483 and oceanographic applications. Bull. Amer. Meteor. Soc., 92, 157-174,
484 doi:10.1175/2010BAMS2946.1.
485 Brink, K. H., 1989: Observations of the response of thermocline currents to a hurricane. J. Phys.
486 Oceanogr., 19, 1017-1022.
487 Chen, G., J. Gan, Q. Xie, X. Chu, D. Wang, and Y. Hou, 2012. Eddy heat and salt transports in the
488 South China Sea and their seasonal modulations, J. Geophys. Res., 117, C05021,
489 doi:10.1029/2011JC007724.
490 Chu, P. C., J. M. Veneziano, C. Fan, M. J. Carron, and W. T. Liu, 2000: Response of the south
491 china sea to tropical cyclone ernie 1996. J. Geophys. Res., 105 (C6), 13 991-14 009.

492 D'Asaro, E. A., 1989: The decay of wind-forced mixed layer inertial oscillations due to the β-
493 effect. J. Geophys. Res., 94 (C2), 2045-2056.
494 D'Asaro, E. A., C. C. Eriksen, M. D. Levine, P. Niiler, C. A. Paulson, and P. V. Meurs, 1995:
495 Upper-ocean inertial currents forced by a strong storm. part I: Data and comparisons with linear
496 theory. J. Phys. Oceanogr., 25, 2909-2937.
497 Danioux, E., P. Klein, and P. Riviere, 2008: Propagation of Wind Energy into the Deep Ocean
498 through Mesoscale Eddy Field. J. Phys. Oceanogr., 38, 2224-2241.
499 Danioux, E., Vanneste, J. and Bühler, O., 2015: On the concentration of near-inertial waves in
500 anticyclones. Journal of Fluid Mechanics, 773.
501 Davies, A. M. and J. Xing, 2002: Influence of coastal fronts on near-inertial internal waves.
502 Geophys. Res. Lett., 29 (23), 2114, doi:10.1029/2002GL015904.
503 Fairall, C. W., E. F. Bradley, J. E. Hare, A. A. Grachev, and J. B. Edson, 2003: Bulk
504 parameterization of air-sea fluxes: Updates and verification for the COARE algorithm, J. Clim.,16
505 (4), 571–591.
506 Ferrari, R., and C. Wunsch, 2009: Ocean circulation kinetic energy: Reservoirs, sources, and sinks.
507 Annual Review of Fluid Mechanics, 41, 253-282.
508 Gan J., Z. Liu and L. Liang, 2016a: Numerical modeling of intrinsically and extrinsically forced
509 seasonal circulation in the China Seas: A kinematic study, J. Geophys. Res. (Oceans), 121 (7),
510 4697-4715, doi: 10.1002/2016JC011800.
511 Gan, J., Z. Liu and C. Hui, 2016b: A three-layer alternating spinning circulation in the South China
512 Sea, J. Phys. Oceanogr. doi:10.1175/JPO-D-16-0044.
513 Gan, J. and J. S. Allen, 2005: On open boundary conditions for a limited-area coastal model off
514 Oregon. part 1: Response to idealized wind forcing. Ocean Modelling, 8, 115-133.

515 Gan, J., H. Li, E. N. Curchister, and D. B. Haidvogel, 2006: Modeling South China Sea circulation:
516 Response to seasonal forcing regimes. J. Geophys. Res., 111 (C06034),
517 doi:10.1029/2005JC003298.
518 Gan, J., and T. Qu, 2008: Coastal jet separation and associated flow variability in the southwest
519 South China Sea. Deep-Sea Res. I, doi:10.1016/j.dsr. 2007.09.008.
520 Garrett, C., 2001: What is the "near-inertial" band and why is it different from the rest of the
521 internal wave spectrum? J. Phys. Oceanogr., 31, 962-971.
522 Geisler, J.E., 1970: Linear theory of the response of a two layer ocean to a moving hurricane.
523 Geophysical and Astrophysical Fluid Dynamics, 1, 249-272.
524 Gill, A. E., 1984: On the behavior of internal waves in the wakes of storms. J. Phys. Oceanogr.,
525 14, 1129-1151.
526 Gonella, J., 1972: A rotary-component method for analysing meteorological and oceanographic
527 vector time series. Deep-Sea Research, 19, 833-846.
528 Gregg, M. C., E. A. D'Asaro, T. J. Shay, and N. Larson, 1986: Observations of persistent mixing
529 and near-inertial internal waves. J. Phys. Oceanogr., 16, 856-885, 21.
530 Hebert, D. and J. N. Moum, 1994: Decay of a near-inertial wave. J. Phys. Oceanogr., 24, 2334-
531 2351.
532 Jing, Z., Wu, L. and Ma, X. 2015: Improve the simulations of near-inertial internal waves in the
533 ocean general circulation models. J. Atmos. Ocean. Technol., 32(10), 1960-1970.
534 Jordi, A. and D.-P. Wang, 2008: Near-inertial motions in and around the Palamos submarine
535 canyon (NW Mediterranean) generated by a severe storm. Continental Shelf Research, 28, 2523-
536 2534.
537 Kundu, P. K. and I. M. Cohen, 2008: Fluid Mechanics, 872 pp. Academic, San Diego.

538 Kunze, E., 1985: Nearinertial wave propagation in geostrophic shear. J. Phys. Oceanogr., 15, 544-
539 565.
540 Liu, L. L., W. Wang, and R. X. Huang, 2008: The mechanical energy input to the ocean induced
541 by tropical cyclones. J. Phys. Oceanogr., 38, 1253-1266.
542 Locarnini, R. A., A. V. Mishonov, J. I. Antonov, T. P. Boyer, and H. E. Garcia, 2006. World Ocean
543 Atlas 2005, Volume 1: Temperature. S. Levitus, Ed. NOAA Atlas NESDIS 61, U.S. Government
544 Printing Office, Washington, D.C., 182 pp.
545 Mooers, C. N. K., 1973: A technique for the cross spectrum analysis of pairs of complex- valued
546 time series, with emphasis on properties of polarized components and rotational invariants. Deep-
547 Sea Research, 20, 1129-1141.
548 Morozov, E. G. and M. G. Velarde, 2008: Inertial oscillations as deep ocean response to hurricanes.
549 Journal of Oceanography, 64(4), 495-509, doi:10.1007/s10872-008-0042-0.
550 Nagai, T., Tandon, A., Kunze, E. and Mahadevan, A., 2015: Spontaneous generation of near-
551 inertial waves by the Kuroshio Front. J. Phys. Oceanogr., 45, 2381-2406.
552 Price, J., 1981: Upper ocean response to a hurricane. J. Phys. Oceanogr., 11(2), 153-175.
553 Qi, H., R. A. de Szoeke, and C. A. Paulson, 1995: The structure of near-inertial waves during
554 ocean storms. J. Phys. Oceanogr., 25, 2853-2871. 22.
555 Rocha, C.B., Wagner, G.L. and Young, W.R., 2018: Stimulated generation: extraction of energy
556 from balanced flow by near-inertial waves. Journal of Fluid Mechanics, 847, 417-451.
557 Sasaki, H., M. Nonaka, Y. Masumoto, Y. Sasai, H. Uehara, and H. Sakuma, 2008: An eddy-
558 resolving hindcast simulation of the quasiglobal ocean from 1950 to 2003 on the Earth Simulator.
559 In High Resolution Numerical Modelling of the Atmosphere and Ocean, K. Hamilton and
560 W. Ohfuchi (eds.), chapter 10, pp. 157–185, Springer, New York.

561 Shay, L. K. and R. L. Elsberry, 1987: Near-inertial ocean current responses to hurricane Frederic.
562 J. Phys. Oceanogr., 17, 1249-1269.
563 Shchepetkin, A. F. and J. C. McWilliams, 2005: The regional ocean modeling system: A split-
564 explicit, free-surface, topography following coordinates ocean model. Ocean Modelling, 9, 347-
565 404.
566 Silverthorne, K. E. and J. M. Toole, 2009: Seasonal kinetic energy variability of near-inertial
567 motions. J. Phys. Oceanogr., 39, 1035-1049.
568 Simmons, H. L. and M. H. Alford, 2012: Simulating the long-range swell of internal waves
569 generated by ocean storms. Oceanography, 25 (2), 30-41, doi:http://dx.doi.org/10.5670/
570 oceanog.2012.39.
571 Sun, L., Q. Zheng, D. Wang, J. Hu, C.-K. Tai, and Z. Sun, 2011a: A case study of near-inertial
572 oscillation in the south china sea using mooring observations and satellite altimeter data. Journal
573 of Oceanography, 67, 677-687, doi:10.1007/s10872-011-0081-9.
574 Sun, Z., J. Hu, Q. Zheng, and C. Li, 2011b: Strong near-inertial oscillations in geostrophic shear
575 in the northern south china sea. Journal of Oceanography, 67, 377-384, doi:10.1007/ s10872-011-
576 0038-z.
577 Thomas, L. N., 2019: Enhanced radiation of near-inertial energy by frontal vertical circulations.
578 J. Phys. Oceanogr., 49, 2407-2421.
579 Wang, G., J. Su, Y. Ding, and D. Chen, 2007: Tropical cyclone genesis over the South China Sea.
580 Journal of Marine Systems, 68, 318–326.
581 Watanabe, M. and T. Hibiya, 2002: Global estimate of the wind-induced energy flux to the inertial
582 motion in the surface mixed layer. Geophys. Res. Lett., 29, 1239, doi:10.1029/2001GL04422. 23.

583 Whitt, D.B. and Thomas, L.N., 2013. Near-inertial waves in strongly baroclinic currents. J. Phys.
584 Oceanogr., 43, 706-725.
585 Xu, Z., B. Yin, Y. Hou, and Y. Xu, 2013: Variability of internal tides and near-inertial waves on
586 the continental slope of the northwestern South China Sea. J. Geophys. Res., 118, 1-15,
587 doi:10.1029/2012JC008212.
588 Young, W. R. and M. B. Jelloul, 1997: Propagation of near-inertial oscillations through a
589 geostrophic flow. Journal of Marine Research, 55, 735-766.
590 Zedler, S. E., 2009: Simulations of the ocean response to a hurricane: Nonlinear processes. J. Phys.
591 Oceanogr., 39, 2618-2634.
592 Zhai, X., R. J. Greatbatch, and J. Sheng, 2004: Advective spreading of storm-induced inertial
593 oscillations in a model of the northwest Atlantic Ocean. Geophys. Res. Lett., 31 (L14315),
594 doi:10.1029/2004GL020084.

List of Table

List of Figures

Figure 1 (a) Track of typhoon Neoguri (2008) from JTWC; blue triangles represent ARGO drifter locations and the red circle represents Wenchang where there were ADCP observations. The date is marked by month/day along the track. TS: tropical storm, STS: strong tropical storm, T: typhoon, ST: strong typhoon, and Super T: super typhoon. (b) translation speed (U_h, unit: m s^{-1}) and the 1st baroclinic wave speed (C_1, unit: m s^{-1}) along the TC track; (c) clockwise (A_{cw}, green line) and counter-clockwise (A_{ccw}, blue line) rotary current amplitude (m s^{-1}) from current measurement at Wenchang. The *x*-axis is time marked as month/day.

Figure 2 Daily mean KE (J m^{-3}, color contour) and current vectors (arrows) at 10 m (a) on April 14 of the pre-storm stage (PS), (b) on April 18 during the strongest wind forcing of the forced stage (FS), (c) on April 20 after the end of the FS, and (d) on April 30 during the relaxation stage (RS). The grey contours are the 200 m, 500 m, and 1000 m isobaths. The magenta line represents TC track. Yellow triangle on April 18 represents the TC location. The TC was located beyond the plotting domain during the other three days, as shown in Figure 1a. The velocity magnitudes<0.2 ms^{-1} are not shown in the vectors.

Figure 3: ΔSST (SSTApril 19-SSTApril14) from (a) model results and (b) GHRSST JPL MUR satellite products. The pink curve refers to the trajectory of the TC Neoguri.

Figure 4 Rotary spectra of clockwise component (upper 10 m) at Wenchang (112°E, 19.6°N) from model simulations (red) and observations (blue).

Figure 5 Time series, represented by color bar, of daily (a) clockwise and (b) counter-clockwise rotary current vectors from April 14 to 30 during different stages of the TC forcing, signifying the response of the current to the local wind rotation. For the clockwise (counter-clockwise)

component, only currents with magnitude larger than 0.2 (0.05) m s^{-1} are shown. The black box represents the forced region.

Figure 6 Time series of 6-hourly wind stress vectors during the forced-stage (FS) from April 15-20.

Figure 7 Time series of (a) the area-averaged wind energy flux into the near-inertial band (unit: 10^{-3} W m^{-2}) and (b) depth-integrated KEni (J m^{-2}) in the forced region for different layers.

Figure 8 Daily averaged KEni (KJ m^{-2}) of layers (a, b) 30-200 m and (c,d) below 200 m on (a, c) April 20 during FS, and (b,d) April 30 during RS. The thick red arrows show the location of the jet stream (Fig. 2), while the orange curve arrows indicate regions with relative vorticity $\zeta > 0$, and the blue curve arrows indicate regions with $\zeta < 0$ induced by the jet. Stations A1 and A2 are on the right side of the TC track at the northern (A2) and southern (A1) sides of the jet, respectively. Stations C1 and C2 are corresponding stations in the far field. Station B is located in the upstream of the jet stream.

Figure 9 Time series of (a, b) u_i (m s^{-1}), (c, d) KEni (J m^{-2}), and (e, f) rotary spectra (cw component) at locations A1 (a,c,e) and A2 (b,d,f).

Figure 10 Time-averaged N^2 (s^{-2}) from April 15 to May 5 at locations A1 (red) and A2 (blue).

Figure 11 As in Fig. 9, except for locations C1 (a, c, e) and C2 (b, d, f).

Figure 12 Time series of area-averaged, depth-integrated KEni budget for (a) 0-30 m, (b) 30-200 m, and (c) >200 m in the forced region. Terms represent (unit: $\times 10^{-3}$ W m^{-2}): (a-c) vertical viscous effect (VVISC), (d-f) divergence of energy flux (PRES), (g-i) horizontal non-linear interaction (NL_h), and (j-l) vertical non-linear interaction (NL_v). The vertical lines separate the pre-storm stage, FS and RS during the TC forcing.

Figure 13 Horizontal distribution of time-averaged (April 15-May 5) depth-integrated KEni budget in different layers: 0-30 m (left column), 30-200 m (middle), and >200 m (right). The terms re

Figure 14 Time series of KEni budget at locations: A1 (a-c), A2 (d-f), C1 (g-i), and C2 (j-l) in layers: 0-30 m (left column), 30-200 m (middle column), and >200 m (right column).

presented are (unit: $\times 10^{-3}$ W m^{-2}): (a-c) VVISC, (d-f) PRES, (g-i) NL_h, and (j-l) NL_v.

TERM	*RATE*		*VVISC*		*PRES*		*NLh*		*NLv*	
Phase	FS	RS	FS	RS	FS	RS	FS	RS	FS	RS
0-30 m	1.15	-0.97	2.15	0.00	-0.65	-0.85	-0.05	-0.10	-0.29	-0.01
30-200m	1.11	-0.44	0.96	-0.19	0.30	-0.16	0.21	-0.18	-0.35	0.10
>200 m	0.23	0.36	-0.02	-0.09	0.26	0.59	0.00	-0.07	-0.01	-0.07
Column	2.51	-1.02	3.10	-0.27	-0.09	-0.42	0.16	-0.35	-0.66	0.02

Table 1. Time integrated KEni budget (unit: $\times 10^3$ J m^{-2}) during the FS and RS.

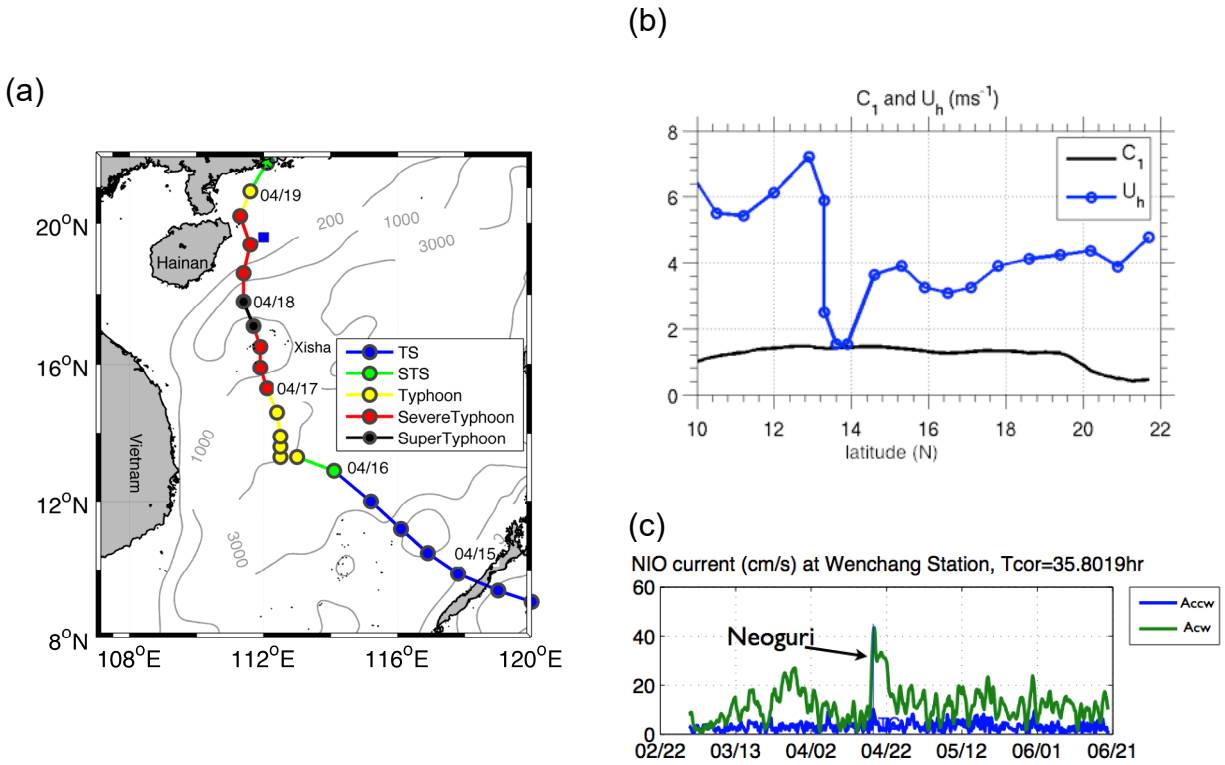

Figure 1 (a) Track of Typhoon Neoguri (2008) from JTWC; blue square represents Wenchang where there were ADCP observations; (b) translation speed (U_h, unit: m s^{-1}) and the 1st baroclinic wave speed (C_1, unit: m s^{-1}) along the TC track; (c) clockwise (A_{cw}) and counter-clockwise (A_{ccw}) rotary current amplitude (m s^{-1}) from current measurement at Wenchang. TS: tropical storm, STS: strong tropical storm.

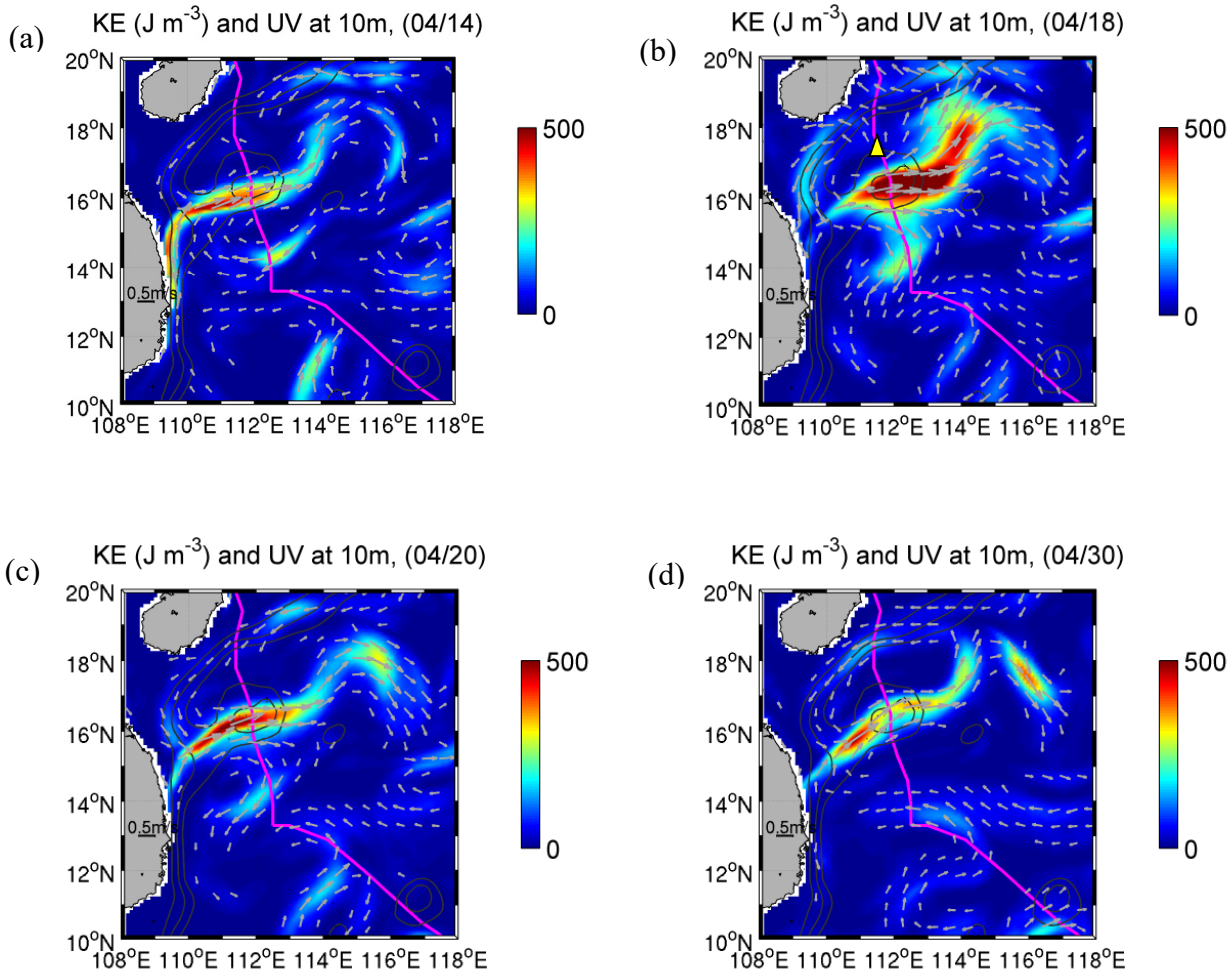

Figure 2 Daily mean KE (J m^{-3}, color contour) and current vectors (arrows) at 10 m (a) on April 14 of the pre-storm stage (PS), (b) on April 18 during the strongest wind forcing of the forced stage (FS), (c) on April 20 after the end of the FS, and (d) on April 30 during the relaxation stage (RS). The grey contours are the 200 m, 500 m, and 1000 m isobaths. The magenta line represents TC track. Yellow triangle on April 18 represents the TC location. The TC was located beyond the plotting domain during the other three days, as shown in Figure 1a. The velocity magnitudes<0.2 ms^{-1} are not shown in the vectors.

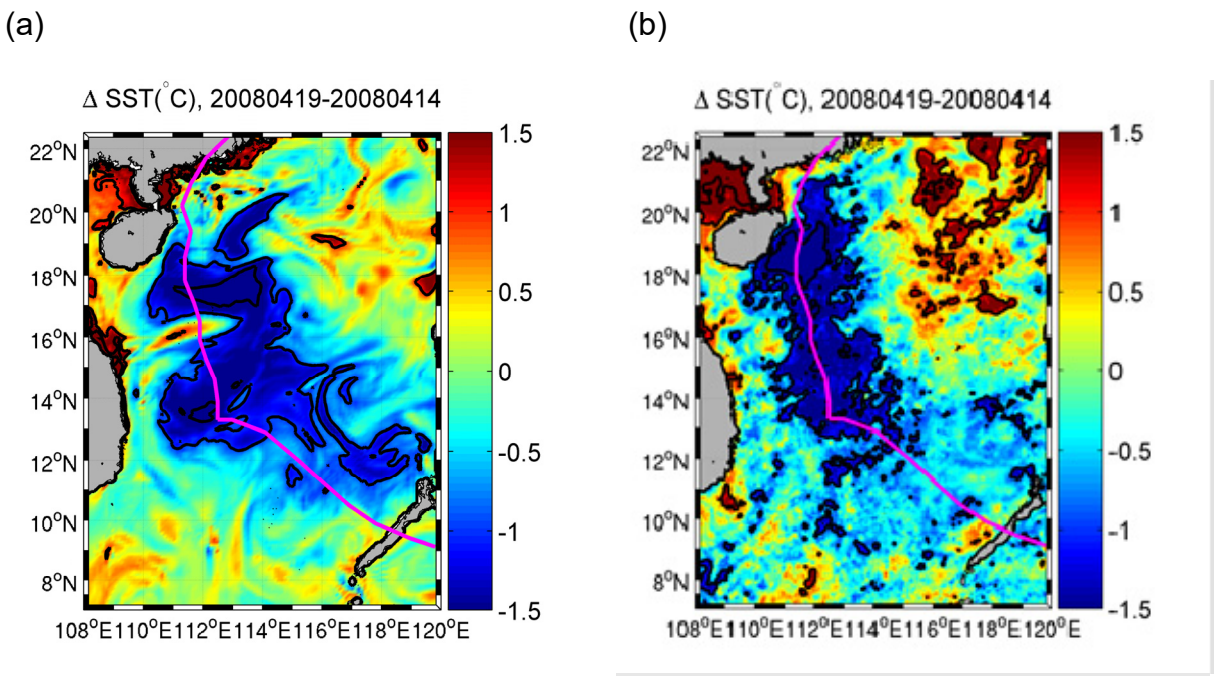

Figure 3 ΔSST ($SST_{April\ 19}$-$SST_{April14}$) from (a) model results and (b) GHRSST JPL MUR satellite products. The pink curve refers to the trajectory of the TC Neoguri.

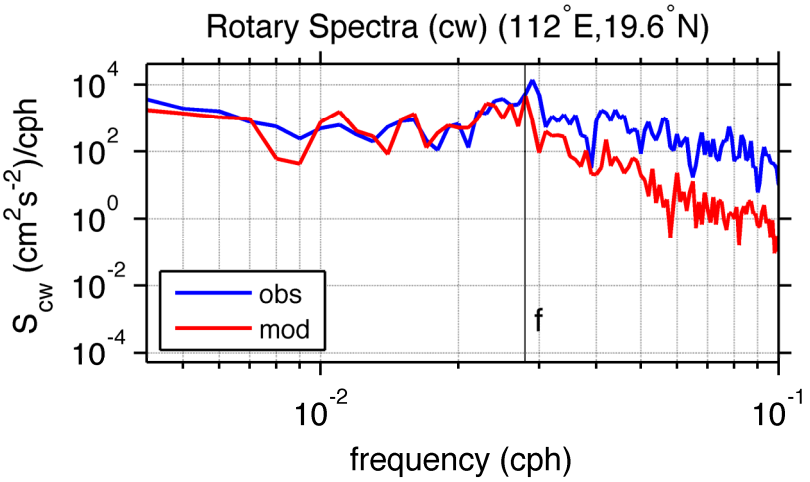

Figure 4 Rotary spectra of clockwise component (upper 10 m) at Wenchang (112°E, 19.6°N) from model simulations (red) and observations (blue).

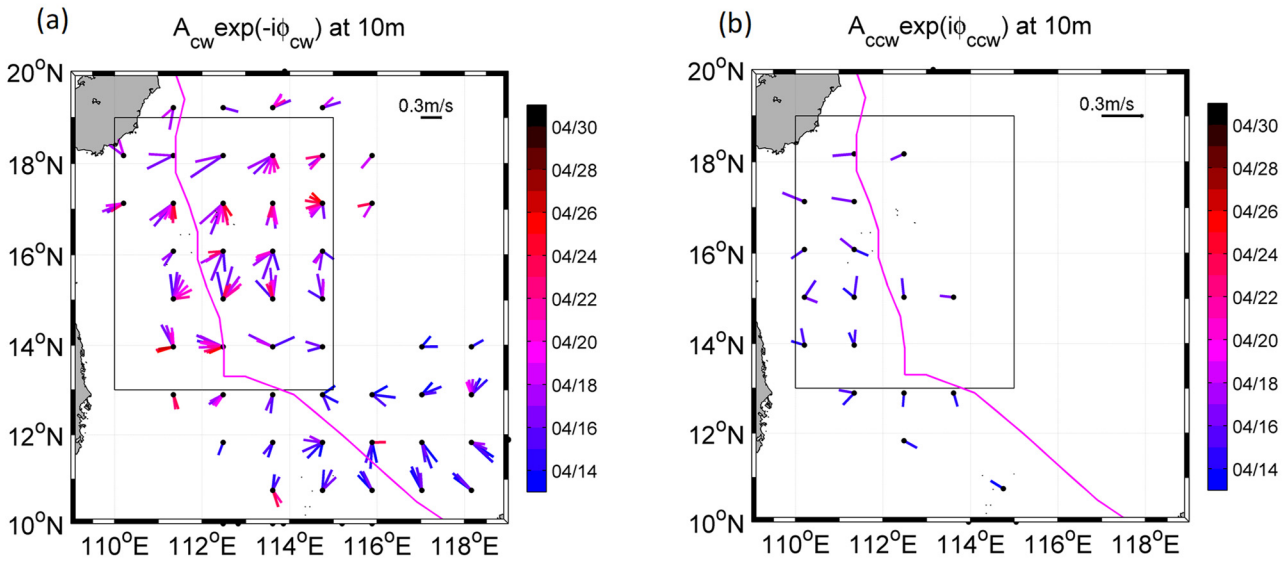

Figure 5 Time series, represented by color bar, of daily (a) clockwise and (b) counter-clockwise rotary current vectors from April 14 to 30 during different stages of the TC forcing, signifying the response of the current to the local wind rotation. For the clockwise (counter-clockwise) component, only currents with magnitude larger than 0.2 (0.05) m s^{-1} are shown. The black box represents the forced region.

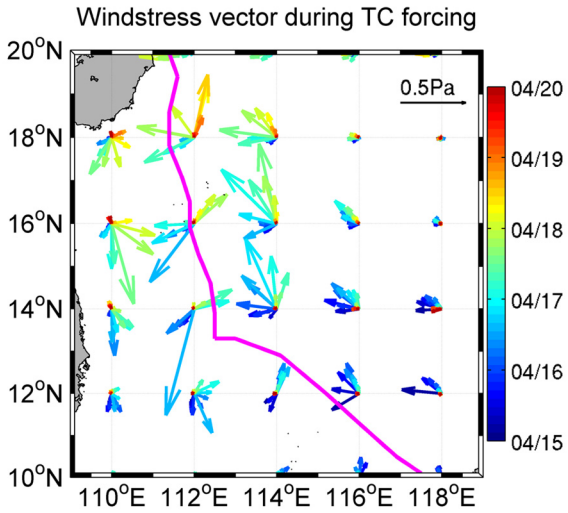

Figure 6 Time series of 6-hourly wind stress vectors during the forced-stage (FS) from April 15-20.

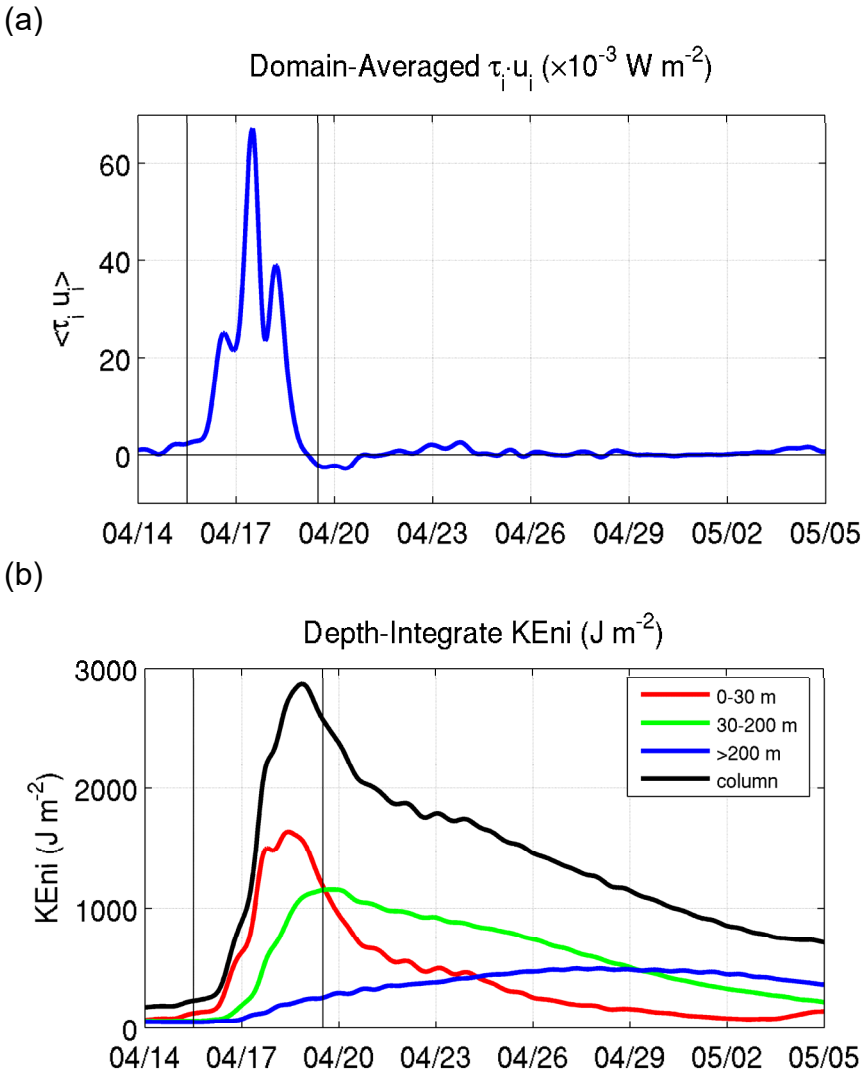

Figure 7 Time series of (a) the area-averaged wind energy flux into the near-inertial band (unit: 10^{-3} W m^{-2}) and (b) depth-integrated KEni (J m^{-2}) in the forced region for different layers.

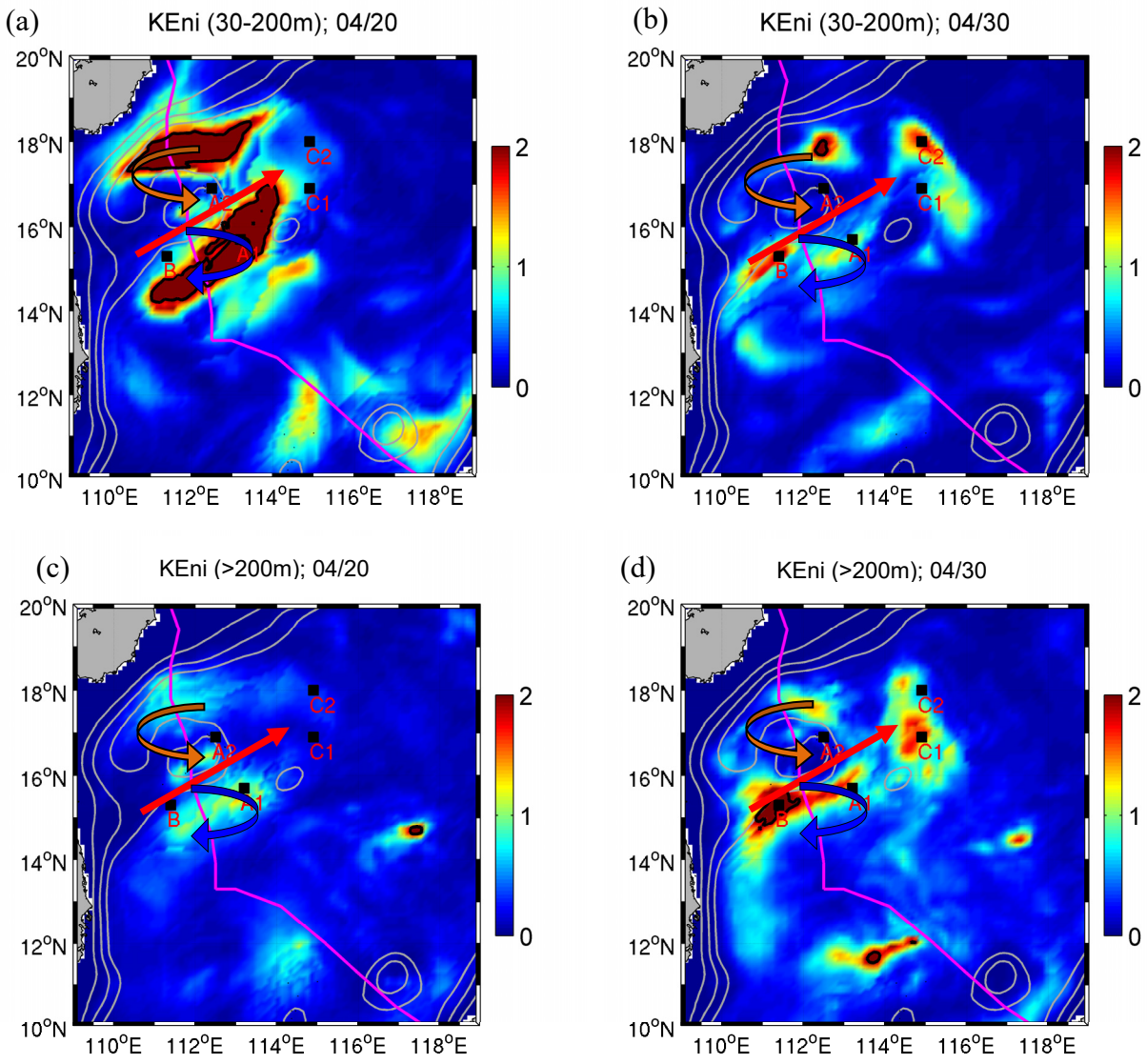

Figure 8 Daily averaged KEni (KJ m^{-2}) of layers (a, b) 30-200 m and (c,d) below 200 m on (a, c) April 20 during FS, and (b,d) April 30 during RS. The thick red arrows show the location of the jet stream (Fig. 2), while the orange curve arrows indicate regions with relative vorticity $\zeta > 0$, and the blue curve arrows indicate regions with $\zeta < 0$ induced by the jet. Stations A1 and A2 are on the right side of the TC track at the northern (A2) and southern (A1) sides of the jet, respectively. Stations C1 and C2 are corresponding stations in the far field. Station B is located in the upstream of the jet stream.

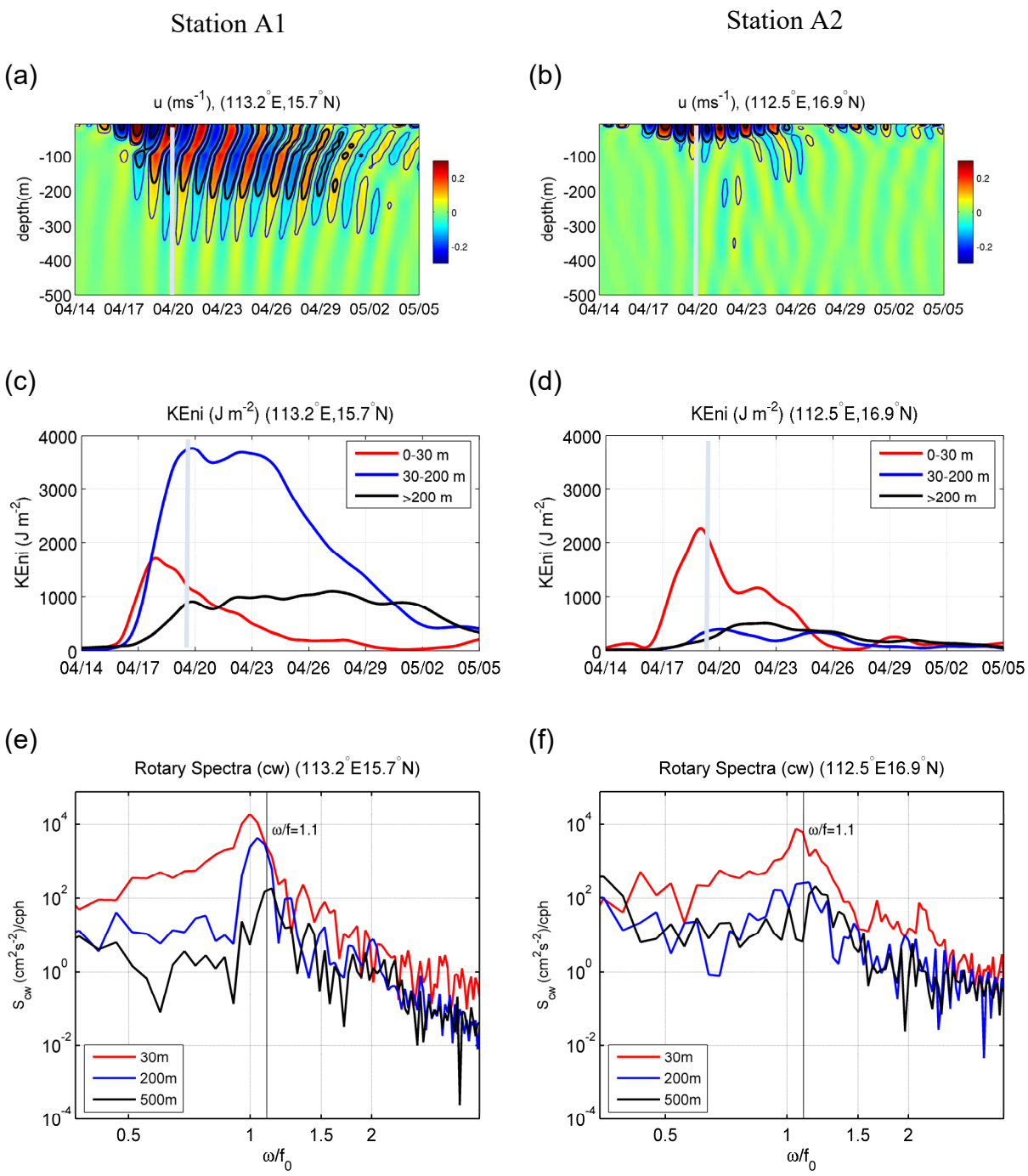

Figure 9 Time series of (a, b) u_i (m s^{-1}), (c, d) KEni (J m^{-2}), and (e, f) rotary spectra (*cw* component) at locations A1 (a,c,e) and A2 (b,d,f).

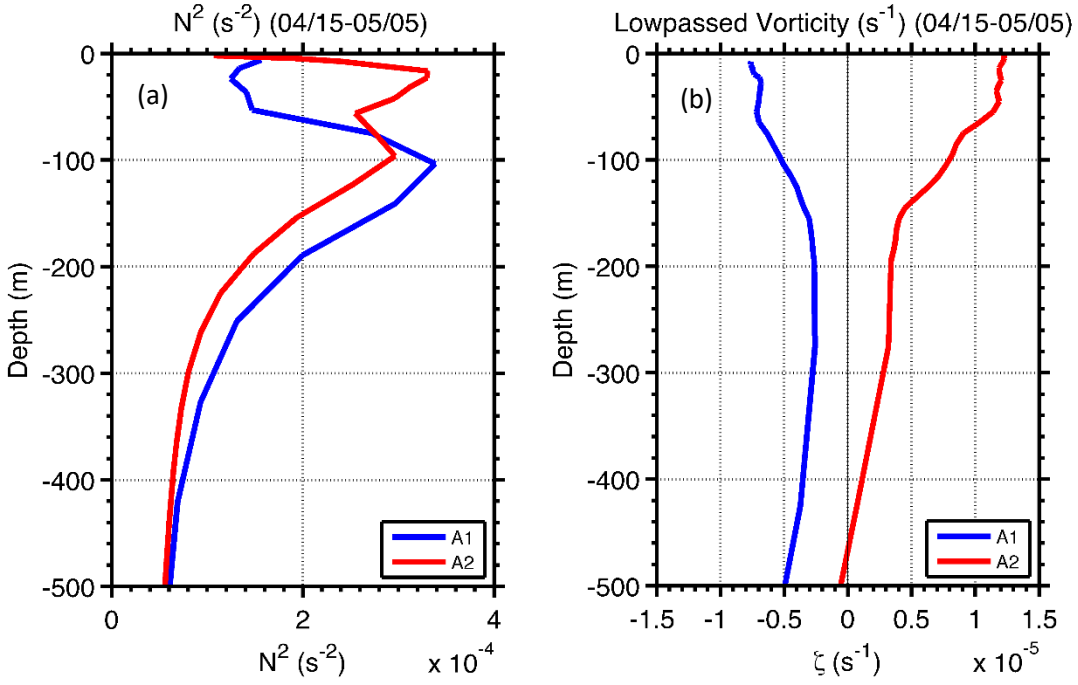

Figure 10 Time-averaged (a) N^2 (s^{-2}) and (b) low-passed (3 day) vorticity from April 15 to May 5 at locations A1 (red) and A2 (blue).

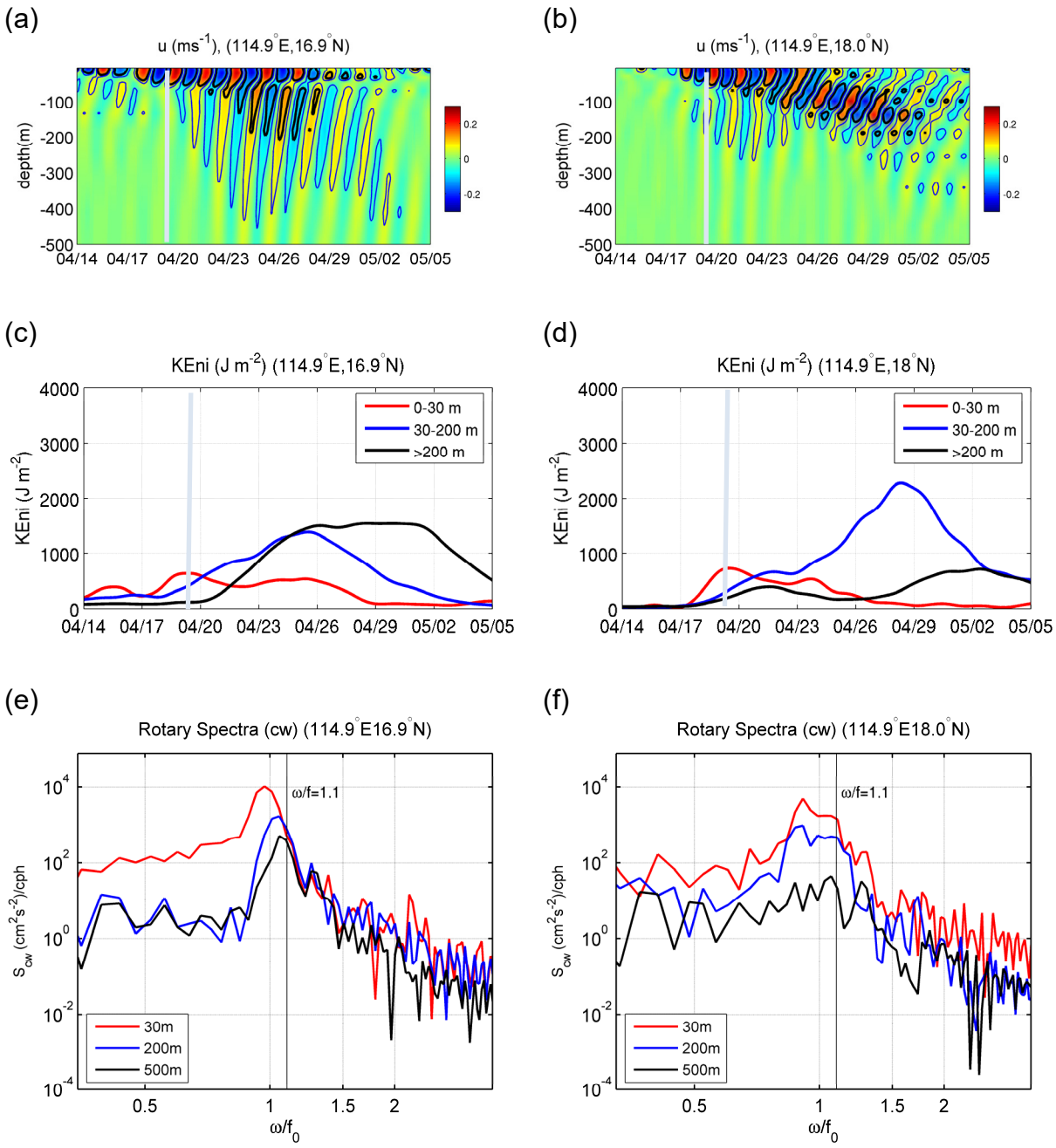

Figure 11 As in Fig. 9, except for locations C1 (a, c, e) and C2 (b, d, f).

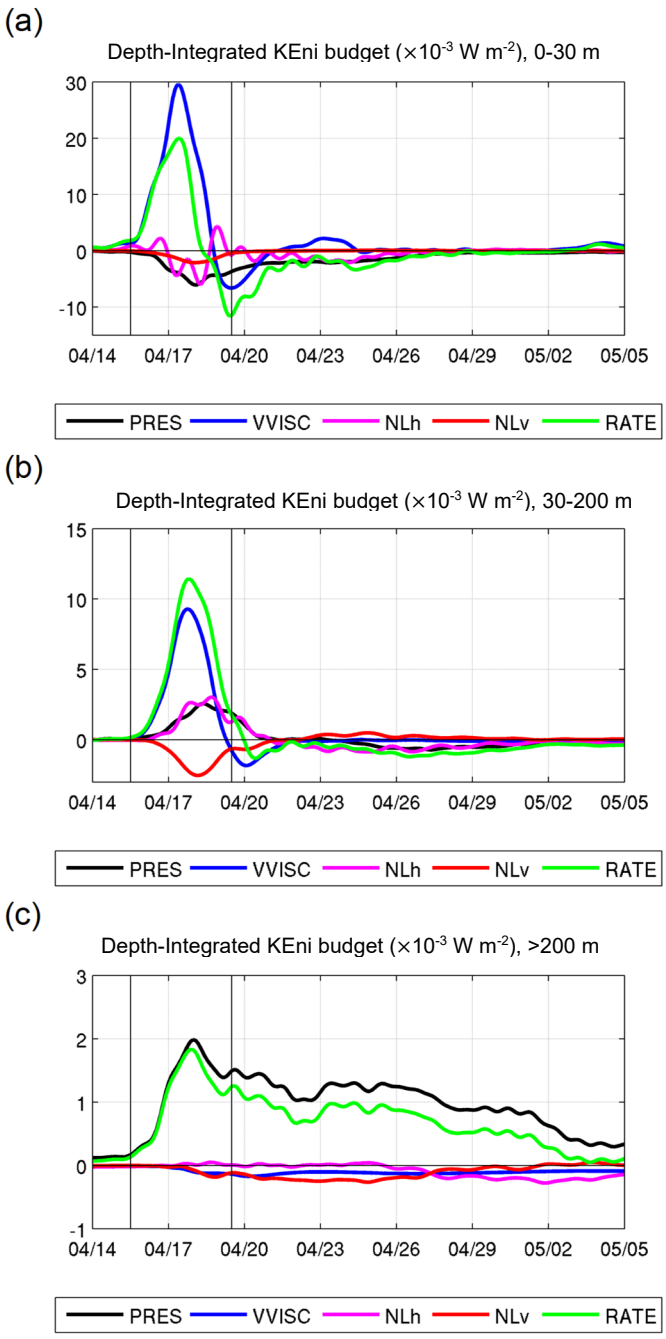

Figure 12 Time series of area-averaged, depth-integrated KEni budget for (a) 0-30 m, (b) 30-200 m, and (c) >200 m in the forced region. Terms represent (unit: $\times 10^{-3}$ W m^{-2}): (a-c) vertical viscous effect (VVISC), (d-f) divergence of energy flux (PRES), (g-i) horizontal non-linear interaction (NL_h), and (j-l) vertical non-linear interaction (NL_v). The vertical lines separate the pre-storm stage, FS and RS during the TC forcing.

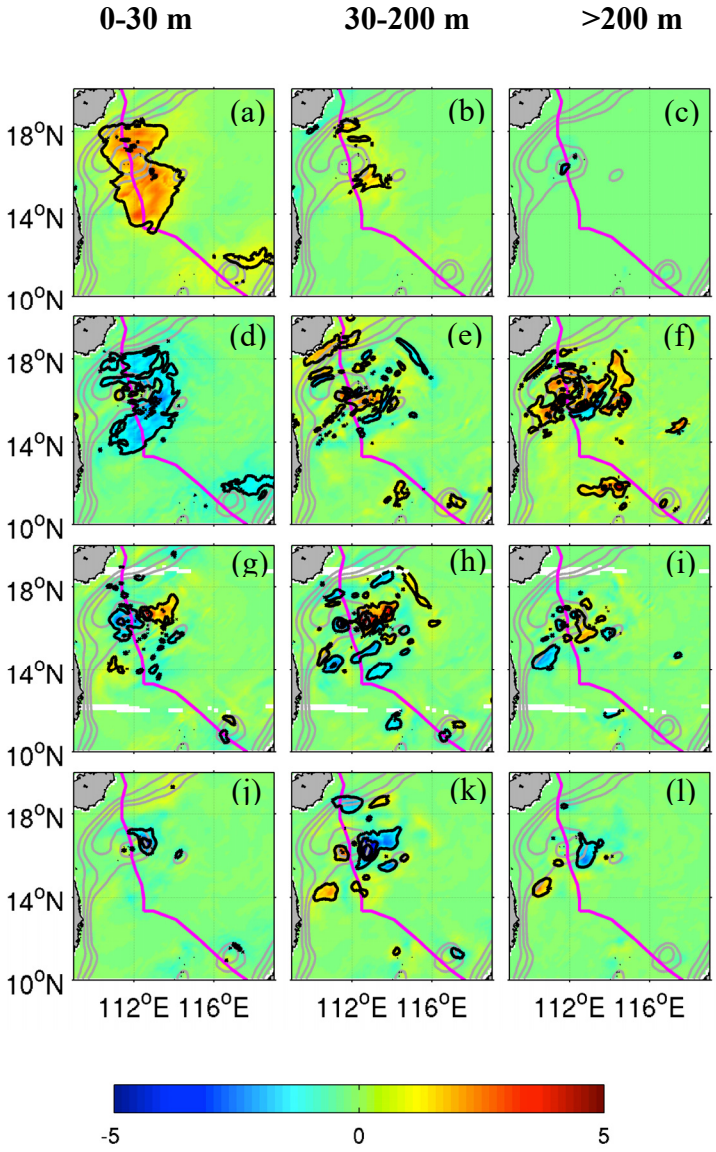

Figure 13 Horizontal distribution of time-averaged (April 15-May 5) depth-integrated KEni budget in different layers: 0-30 m (left column), 30-200 m (middle), and >200 m (right). The terms represented are (unit: $\times 10^{-3}$ W m^{-2}): (a-c) *VVISC*, (d-f) *PRES*, (g-i) NL_h, and (j-l) NL_v.

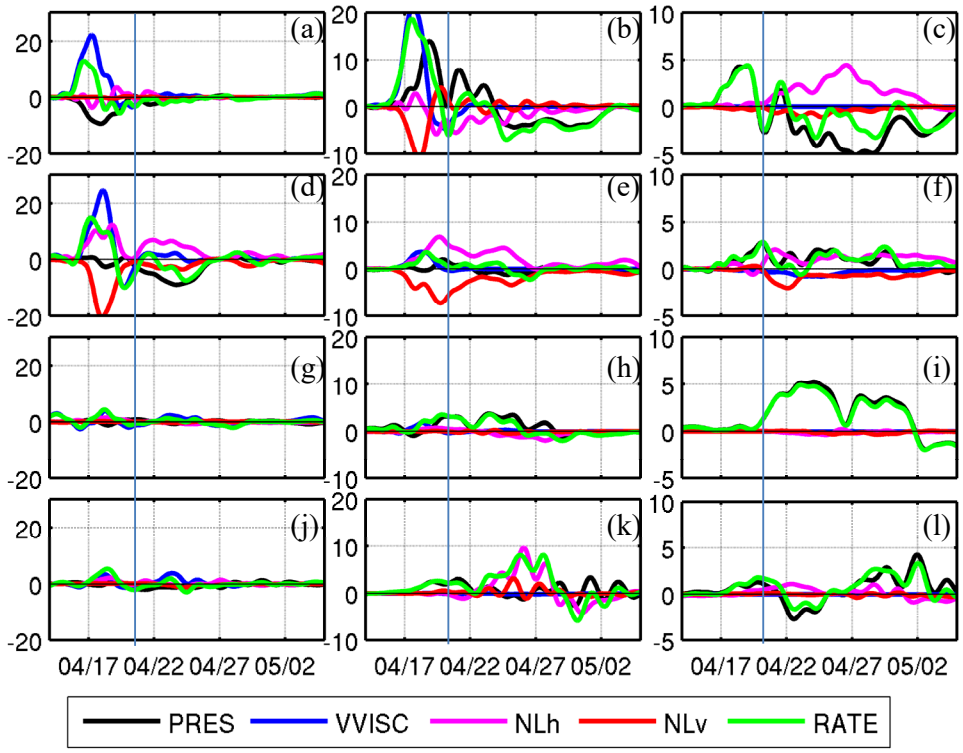

Figure 14 Time series of KEni budget at locations: A1 (a-c), A2 (d-f), C1 (g-i), and C2 (j-l) in layers: 0-30 m (left column), 30-200 m (middle column), and >200 m (right column).